Smoke Detection and Combustion Analysis Using Millimeter-Wave Radar Measurements

Francesca Schenkel, *Graduate Student Member, IEEE*, Thorsten Schultze, Christoph Baer, *Senior Member, IEEE*, Jan C. Balzer, *Member, IEEE*, Ilona Rolfes, *Senior Member, IEEE*, and Christian Schulz, *Member, IEEE*

***Abstract*— Understanding and detecting smoke effectively is crucial in emergency scenarios where traditional optical methods may fail. This article investigates the definition of smoke and its characterization from an electromagnetic perspective, focusing particularly on the use of frequency-modulated continuous wave (FMCW) radar sensors operating in the millimeter-wave range. We explore the influence of both laminar and turbulent smoke flows on the measurement accuracy. Our study is grounded in dielectric models in the millimeter-wave spectrum, demonstrating that the dielectric properties of smoke exhibit minimal variations. Consequently, we use phase-based radar signal processing to detect these subtle changes. Unlike previous studies that primarily evaluate sensor performance, this article aims to use the minimal impact on the measured signal to characterize different smoke scenarios comprehensively. Our findings demonstrate that radar sensors can provide valuable insights into smoke properties and are suitable to extend material model for millimeter-wave frequencies, enhancing situational awareness and response strategies in smoke-obscured environments.**

***Index Terms*— Combustion, frequency-modulated continuous wave (FMCW), gas permittivity, radar measurements, smoke meteorology, *W*-band.**

I. Introduction

FIRE detection technologies have seen significant advancements, yet the development of effective fire detection systems remains a critical research and industrial topic due to false alarms. A major challenge in fire detection is the diverse range of environments and conditions where fires can occur, such as residential buildings, industrial plants, forests, or public buildings. This diversity makes it difficult to develop a universal system effective in all scenarios. Consequently, research focuses on creating innovative approaches and technologies to enhance fire detection versatility and effectiveness. This includes early detection of potentially dangerous situations while minimizing false alarms through the integration of sensors, artificial intelligence, and machine learning. Traditional smoke detectors typically use optical sensors to detect airborne smoke particles, resulting in the activation of an alarm when smoke particles in a certain amount are detected. But they are prone to false alarms. Collecting statistics on the false alarm rate of smoke detectors is difficult, as the definition of a false alarm varies from country to country. Generally, it is observed that in many countries, such as Germany, Switzerland, and Sweden, false alarm rates exceed 90%. This includes manual activation for both good and malicious reasons. In Sweden, detailed statistics on false alarms reveal that 20% of the false alarm were triggered by smoke during cooking, over 6% by water vapor, and for over 30% the reason for activation is not known [1]. Therefore, in areas with high levels of dust or humidity, heat detectors are used that respond to an increase in room temperature. Video-based fire detection [2] is another method, although it may not be suitable for private households, due to privacy concerns. If a fire needs to be extinguished in a public place, a combination of a video surveillance system and an infrared camera can be used to locate people or animals and determine the temperature of the fire. However, studies have shown that hot smoke formations make it difficult to detect people, as the different temperatures of the smoke and the individuals cannot be distinguished from each other [3]. This makes it difficult to obtain information about what is happening behind the smoke. Successful firefighting requires the protection of not only the public but also the emergency services. For this reason, there is growing interest in the use of reconnaissance units such as drones or robots [4]. Ideally, they should be able to perform imaging, material characterization, and vital signs' detection without losing their orientation. The successful development of such applications requires a combination of different sensors for redundancy and diversity. In particular, radar sensors are outstanding: when laser- and video-based orientation systems fail in smoke environments, radar sensors are still capable of determining the distance to objects without notable performance degradation in harsh environments [5], [6]. Advances in research show that radar sensors are not only ideal for orientation but can also be used for imaging [7], material characterization [8], [9], [10], and life-sign detection [11]. However, the presence of smoke plumes causes a change in the dielectric properties of the measurement path, which affects the measurement signal. For the overall quality and functionality of a radar sensor, the

Received 7 July 2024; revised 13 September 2024; accepted 6 October 2024. Date of publication 30 October 2024; date of current version 7 January 2025. This work was supported by Deutsche Forschungsgemeinschaft (DFG, German Research Foundation) under Project 287022738-TRR 196, Project M02 and M05, and Project 422037413–CRC/TRR 287 "BULK-REACTION." An earlier version of this article was presented at the 2024 IEEE/MTT-S International Microwave Symposium (IMS), Washington, DC, USA, June 16-21, 2022 [DOI: 10.1109/IMS40175.2024.10600292]. *(Corresponding author: Francesca Schenkel.)*

Francesca Schenkel, Ilona Rolfes, and Christian Schulz are with the Institute of Microwave Systems, Ruhr University Bochum, 44801 Bochum, Germany (e-mail: francesca.schenkel@rub.de).

Thorsten Schultze and Jan C. Balzer are with the Chair of Communication Systems, University of Duisburg–Essen, 47057 Duisburg, Germany.

Christoph Baer is with the Institute of Electronic Circuits, Ruhr University Bochum, 44801 Bochum, Germany.

Color versions of one or more figures in this article are available at https://doi.org/10.1109/TMTT.2024.3479218.

Digital Object Identifier 10.1109/TMTT.2024.3479218

impact of smoke must be analyzed. As mentioned earlier in [5] and [6], the studies [12] and [13] show that it is possible to determine distance through fire and smoke using millimeter-wave radar sensors. However, when switching to a phase-based signal processing approach, there is a significant change in the measured phase over time. These changes can be crucial for imaging or life-sign detection. This work is an extension on our research in [13] and attempts to improve the understanding of the interaction between electromagnetic waves and smoke. Therefore, smoke is described by its dielectric characteristics, which is defined by a gas–particle mixture. Hence, the changing gas state and the airborne particles must be considered separately. The next step was the extraction of the dielectric properties of the surrounding air mixture change during a fire. This knowledge is then combined with the upcoming particles of the incomplete combustion. Finally, the additional effect of temperature on the gases was simulated. To ensure repeatable and controllable measurements, these were conducted in a laboratory designed in accordance with the European Standard EN54-7. It allows for the measurement of well-defined laminar smoke in the smoke duct and to ignite controlled fires in a large-scale laboratory to measure smoke plumes with a turbulent flow profile. Three different measurement scenarios are considered here.

1) Laminar flow measurements in a smoke duct.
2) Smoke generator in an open room for turbulent flow measurements.
3) Test fires (TFs) in a fire detection laboratory for smoke measurements as realistic scenario.

With these three measurement scenarios, precise measurements of the dielectric properties of the smoke can be made in the smoke duct using frequency-modulated continuous-wave (FMCW) radar sensors. To better simulate a real-life scenario where smoke behaves unpredictably, a smoke generator is used in an open room. Through the observation of different TFs, the turbulent flow behavior of the ascending smoke can be measured over time by phase-based radar measurements. Although the radar sensor measures the rising smoke clearly above the ignited fire, the measured phase pattern over time can be used to draw conclusions about the combustion behavior of the fire. In summary, this article aims to provide a better understanding of the interactions between smoke and electromagnetic waves and how modern radar technologies can contribute to improve smoke detection and combustion characterization. This article is structured as follows, Section II describes the primary mechanisms governing the dielectric properties of smoke and their effect on radar signals. Section III provides a brief overview of standardized laboratory setups and smoke characteristics. Then, in Section IV, measurements are presented and discussed. Finally, Section V provides concluding remarks.

II. Dielectric Properties of Smoke

To understand the influence of smoke on electromagnetic signals and to determine its dielectric properties, it is essential to define smoke. Smoke is a suspension of airborne particulates, such as aerosols or fine dust, and gases emitted when material undergoes combustion or pyrolysis, together with the surrounding air that becomes mixed into the upcoming gases. It is apparent that describing smoke from an electromagnetic point of view is not an easy undertaking. It is a multiphysical process, which has various chemical components, elements of different aggregate states, and a strong change in temperature. However, to enable a dielectric characterization of smoke, the complex medium of smoke is reduced to three main aspects [14]:

1) the gas mixtures;
2) the particulates;
3) the temperature.

An all-encompassing dielectric model for smoke is difficult to establish. Therefore, a combination of two models is used in this work. First, the gas is considered separately and described using the Debey equation. This model considers the polarizability and dipole moments of the various molecules in the gas mixture and uses these to calculate the relative permittivity. However, this consideration is not sufficient, as the influence of the particulates was neglected. Therefore, electromagnetic mixing formulas are used, which define a homogeneous surrounding material in which homogeneously distributed spherical inclusions are located. In the case of smoke, this means that the surrounding material is the gaseous mixture and the particulates are the inclusions in the gaseous mixture. The aspect of changing temperature is taken up and explained in Section II-C.

A. Dielectric Properties of Gases at mmWave Frequencies

The propagation of electromagnetic waves is significantly influenced by the relative permittivity of the medium through which they propagate. The focus here is on the gas mixture defined by air and gases created by the combustion, which have a significant influence on the composition of the surrounding medium. The interaction of electromagnetic waves with materials can be described by numerous physical phenomena. These mechanisms are indistinguishable from a macroscopic point of view. Therefore, the relative permittivity ε_r is used as a measure to describe these effects. In addition to the relative permittivity, the refractive index n is used for the dielectric analysis of gases. Theoretically, the wavelength dependence of the refractive index can be determined via the electrical susceptibility. As the relative permittivity is also directly linked to the electrical susceptibility, a correlation can be drawn with the refractive index

$$n = \sqrt{\varepsilon_r \mu_r} \tag{1}$$

with μ_r describing the relative permeability of materials. In this context, $\mu_r = 1$ is set, as no magnetizable gases are considered. The refractive index of gases is generally very low. Therefore, the refractivity N is generally used for gases

$$N = (n - 1) \cdot 10^6. \tag{2}$$

As already mentioned, the relative permittivity and thus also the refractive index are a macroscopic description of various polarization mechanisms [15]. From a microscopic point of view, these occur at different frequencies to varying extents.

1) Electronic polarization, which involves the displacement of electron clouds, is significant in the optical and ultraviolet (UV) regions.
2) Ionic polarization, which involves the displacement of positive and negative ions, is significant in the infrared range.

3) Orientation polarization, which involves the alignment of permanent dipoles, is significant in the microwave and lower frequency ranges.

If all the contributors are taken into account by their respective polarizability α and added together, the refractive index can be calculated using the so-called Debye equation [16]

$$\frac{n^2-1}{n^2+2}=\frac{\varepsilon_\mathrm{r}-1}{\varepsilon_\mathrm{r}+2}=\frac{\rho}{3\varepsilon_0}\cdot(\alpha_\mathrm{ori}+\alpha_\mathrm{ion}+\alpha_\mathrm{ele}) \tag{3}$$

with ρ describing the number of particles, ε_0 the dielectric constant of free space, α_ori the orientation polarization, α_ion the ionic polarization, and α_ele the electronic polarization. In the context of gases, this can be simplified to

$$n^2-1=\frac{\rho}{3\varepsilon_0}\cdot(\alpha_\mathrm{ori}+\alpha_\mathrm{dis}). \tag{4}$$

Since only temperature-dependent dipole interactions occur in the mmWave range, only α_ori contributes to the refractive index as a frequency-dependent component. The application of molecular spectroscopic information enables the determination of the refractive index n_dp caused by the dipole interaction with electromagnetic radiation

$$n_\mathrm{dp}=1+2c_0\rho\cdot\sum_j\frac{M_j}{\omega_j^2-\omega^2}\cdot f_\mathrm{L} \tag{5}$$

where M_j indicates the intensity of the jth spectral line of the gas under consideration. The corresponding resonance frequency ω_j marks the transition between the rotational energy levels and ω describing the used frequency of the electromagnetic wave. The molecular spectroscopic information such as M_j, ω_j or f_L can be obtained from the HITRAN [17] database for various molecules. Under atmospheric conditions, a Lorentzian line shape can be assumed for the course of the refractive index. For mmWave frequencies, a van Vleck–Weisskopf [18] line shape is advantageous

$$f_\mathrm{L}=1-\frac{\Delta\omega_j^2\omega}{8\omega_j^2}\left(\frac{\omega_j+\omega}{(\omega_j-\omega)^2+\frac{\Delta\omega_j^2}{4}}-\frac{\omega_j-\omega}{(\omega_j+\omega)^2+\frac{\Delta\omega_j^2}{4}}\right) \tag{6}$$

with $\Delta\omega_j$ describing the half-width of the respective resonance line. The total refractive index n_tot can now be calculated as follows:

$$n_\mathrm{tot}(\omega)=1+(n-1)+(n_\mathrm{dp}(\omega)-1). \tag{7}$$

The total effective refractive index $n_\mathrm{tot,eff}$ of a mixture of different materials can be adequately described by the sum of the refractive indices $n_{\mathrm{tot},k}$ of the constituents, weighted by their volume fraction ζ_k [19]

$$\frac{n_\mathrm{tot,eff}^2(\omega)-1}{n_\mathrm{tot,eff}^2(\omega)+2}=\sum_k\zeta_k\frac{n_{\mathrm{tot},k}^2(\omega)-1}{n_{\mathrm{tot},k}^2(\omega)+2}. \tag{8}$$

In Fig. 1, the frequency dependence of the refractive index can be seen using the example of three molecules. The values for spectral line intensity and spectral line width were modified to align with the temperature and pressure conditions of the controlled room fire as presented in [20]. First, it shows the polar components of air, oxygen (O_2), and water vapor (H_2O), which exhibit different resonance lines at different frequencies.

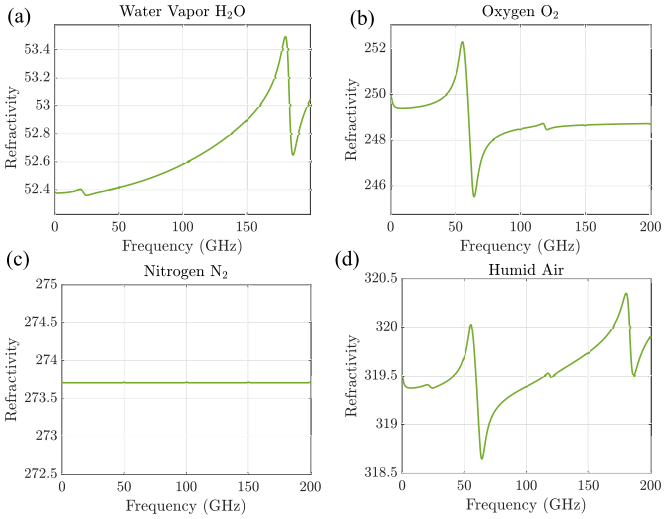

Fig. 1. Simulation of the frequency-dependent refractivities for 325 Pa and 20 °C of (a) water vapor, (b) oxygen, (c) nitrogen, and (d) humid air in a volume fraction like in Table I.

TABLE I

CALCULATED REFRACTIVITIES OF VARIOUS GASES AND SIMULATED REFRACTIVITIES FOR DIFFERENT GAS MIXTURES

Atom Molecule	N[a]	Vol% dry air[a]	Vol% humid air[b]	Vol% combustion product[c]
N_2	273.71	78.09%	77.19%	77.19%
O_2	248.05	20.95%	20.71%	4.5 - 20.71%
Ar	258.11	0.927%	0.916%	0.916%
CO_2	457.79	0.033%	0.033%	0.033 - 12.5%
H_2O	4556.92	0%	1.15%	1.15%
CO	325.21	0%	0%	0 - 1.15%
N	-	268.10	317.61	317.61 - 403.2

[a] Refractivity when 100% of the gas exists on the molecule under consideration
[b] for 101 325 Pa and 20°C and 80 GHz.
[c] from a real room fire [20].

Second, it shows the nonpolar molecule nitrogen (N_2), which is almost constant over the entire simulated frequency. The other components of the air mixtures such as argon (Ar) and carbon dioxide (CO_2) are also nonpolar and have a similar frequency curve. Finally, the refractive index of humid air was calculated, which has resonance lines at similar positions due to the available polar elements O_2 and H_2O. A summary of the volume fractions of dry air and humid air can be found in Table I. It can be clearly observed that at a relative humidity of 50%, the absolute amount of water vapor in the air is just under 1%. However, in terms of the refractivity of air, the percentage of water vapor is almost 20%.

The influence of combustion on the ambient air mixture will now be discussed in more detail. From a chemical perspective, combustion is an exothermic redox reaction in which a fuel is oxidized by an oxidizing agent, usually atmospheric oxygen. The reaction products are typically gaseous, but incomplete combustion can result in aerosols and particulates. To understand how the gas mixture can change during combustion, the refractivity of a controlled room fire described in [20] is calculated in Table II. Under controlled conditions, gas concentrations were measured under the ceiling of a fully equipped room. In total, 22 different gases and substances

TABLE II
GAS CONCENTRATIONS DURING A CONTROLLED ROOM FIRE ACCORDING TO [20] AND THE RESULTING REFRACTIVITY

Time	10 Min.	12 Min	13.6 Min	14 Min	16 Min
N_2	77.19%	77.19%	77.19%	77.19%	77.19%
O_2	19.44%	18.76%	9.95 %	6.1%	20.21
Ar	0.916%	0.916%	0.916%	0.916%	0.916%
CO_2	0.97%	1.62%	11.61%	6.48%	0.81%
H_2O	1.15%	1.15%	1.15%	1.15%	1.15%
CO	0%	0%	1.65%	0.31%	0%
Remaining	0.46%	0.7%	3.16%	1.92%	0%
N	322.81[a]	325.67[a]	402.71[a]	384.65[a]	321.02[a]

[a] the refractivity for the remaining gases: N = 1000 (later adapted to the volume fraction in the gas mixture), also: T= 20°C and p=101 325 Pa

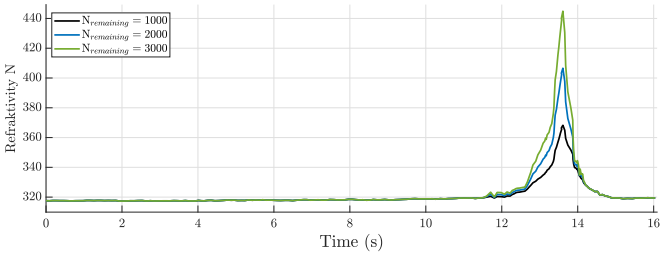

Fig. 2. Simulated refractivity of a controlled room fire according to [20] for different refractivity values for the remaining gases.

were measured. However, it turned out that the greatest change in gas concentration was in O_2, CO_2 and carbon monoxide (CO). These are the main elements of the redox reaction. Table II summarizes the time profile of the changing concentration of O_2, CO_2, and CO and the combined concentration of the 19 other gases measured. These are referred as "remaining gases" below.

In basic terminology, O_2 in the surrounding air is consumed and CO_2 is produced. In addition, starting from the 12th minute, other reaction products such as CO, methane, ethylene, and other inorganic gases begin to form. For the remaining gases, it is difficult to give an exact indication of the refractivity, which is why three different values were assumed for these as examples in Fig. 2. Approximately one-third of the remaining gases consist of the 19 gases listed in the source [20], while two-thirds are unknown. A key aspect of combustion is the production of water vapor, which is a common byproduct of the oxidation process. Although the exact volume fraction of water vapor was not measured, it is reasonable to assume that its proportion increases during the combustion process. In the context of Table II, the increased volume fraction of water vapor caused by combustion is represented as part of the "remaining gases" category. To address the uncertainty in the exact water vapor concentration, we assumed three different refractivity values ($N = 1000$, 2000, and 3000) for the remaining gases in Fig. 2 to illustrate the potential impact on the overall refractivity. While the table shows a constant 1.15% for water vapor, this value should be interpreted as a baseline or minimum concentration, acknowledging that the true value might be higher due to the combustion process. The aim here is not to calculate an exact permittivity but to indicate trends. Literature values show that ethane has a refractivity value of $N = 712$ [21] and acetylene has a value of $N = 879$ [21], supporting the plausibility of these assumed values. It is clear that the change in gas chemistry plays an important role in the change in relative permittivity. However, the increasing temperatures caused by the fire have not yet been addressed. These are explained in Section II-C.

B. Dielectric Properties of Gas and Particulates

So far, pure gas permittivities have been considered and the Debye model was sufficient enough. However, since smoke is a gas–particle mixture, another model must be found. Studies such as [22], [23] and [24] show that dielectric mixture formulas represent this scenario very well. The aim of mixing theory is to homogenize the refractive index of gas or gas–solid mixtures as a macroscopic parameter, so that more complicated microscopic description of individual distributions can be omitted. Sihvola [25] compiled a variety of mixing equations for diverse applications. However, most of these equations assume that particles of a secondary material are embedded within a surrounding material. The following considerations will be based on the so-called universal mixing rule, which is expressed as follows:

$$\frac{n_{\text{eff}} - n_{\text{e}}}{n_{\text{eff}} + 2n_{\text{e}} + \nu(n_{\text{eff}} - n_{\text{e}})} = \frac{\zeta \cdot (n_{\text{i}} - n_{\text{e}})}{n_{\text{i}} + 2n_{\text{e}} + \nu(n_{\text{eff}} - n_{\text{e}})}. \tag{9}$$

In (9), the parameters n_{e} and n_{i} represent the refractive index of the surrounding material and the refractive index of the inclusions, respectively. In addition, ζ denotes the volume fraction of the inclusion material, while ν is a selection parameter that defines various mixing models. Nevertheless, the model has some limitations. It assumes that the wavelength of the emitted electromagnetic wave is significantly greater than the diameter of the particles, allowing the size and shape of the individual particles to be neglected, as these do not influence the electromagnetic fields. To define the parameters of ν more precisely, for the homogenization of the smoke, the flying particles are defined as the inclusions, which in turn are enclosed by the gas just determined in Section II-A. With this a piroi information, $\nu = 0$ can be set. This results in the Maxwell–Garnett mixing formula from the general mixing formula, which results in n_{eff} to

$$n_{\text{eff}} = n_{\text{e}} + \frac{3 \cdot \zeta \cdot n_{\text{e}} \cdot (n_{\text{i}} - n_{\text{e}})}{n_{\text{i}} + 2 \cdot n_{\text{e}} - \zeta(n_{\text{i}} - n_{\text{e}})}. \tag{10}$$

C. Temperature Dependence

The data in the HITRAN database were recorded for the reference temperature $T = 296$ K and a pressure of 101 325 Pa. So that the data can also be used for scenarios beyond the standard parameters, and the spectral line intensity M_j and the half-width of the resonance line $\Delta\omega_j$ of the spectral lines must be adapted to the new temperature and the new pressure. M_j can be adjusted using the following expression [17]:

$$M_j = M_j(T_{\text{ref}}) \cdot \frac{Q(T_{\text{ref}})}{Q(T)} \cdot \frac{e^{\frac{-c_2 E''}{T}}}{e^{\frac{-c_2 E''}{T_{\text{ref}}}}} \cdot \frac{1 - e^{\frac{-c_2 \omega_j}{T}}}{1 - e^{\frac{-c_2 \omega_j}{T_{\text{ref}}}}} \tag{11}$$

where T_{ref} is the reference temperature of the database, Q is the total partition sum, E'' is the energy of the lower state, and c_2 is the second radiation constant, which represents the

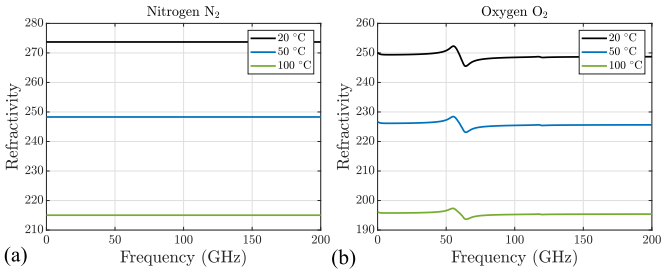

Fig. 3. Simulation of the frequency- and temperature-dependent refractivities of (a) nitrogen and (b) oxygen, all components are simulated for 101 325 Pa at temperatures of 20 °C, 50 °C, and 100 °C.

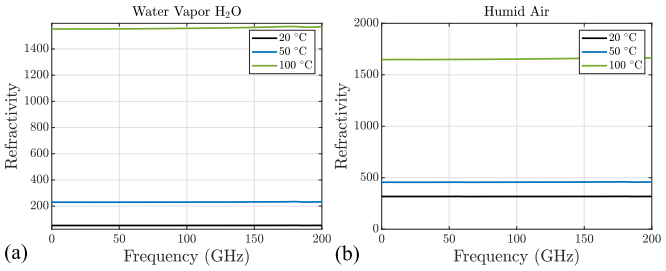

Fig. 4. Simulation of the frequency- and temperature-dependent refractivities of (a) water vapor and (b) humid air like given in Table I, all components are simulated for 101 325 Pa at temperatures of 20 °C, 50 °C, and 100 °C, and the resulting different gas fractions.

relationship between Plank's constant h, the speed of light c_0, and the Boltzmann constant k_B

$$c_2 = hc_0/k_B = 1.43877\text{cmK}. \tag{12}$$

As before, these parameters can also be taken from the HITRAN database. The scaling from room temperature to higher temperatures is sufficiently accurate to estimate the line intensity at higher temperatures. If temperatures of over 1000 K are reached, the HITEMP [26] data should be used. Because in case of excessively high temperatures, there may be significantly more spectral lines, which can be explained by an excited state of the molecules.

$\Delta\omega_j$ is not only temperature-dependent, but also pressure-dependent. For a gas that is exposed to an ambient pressure of p and a temperature T and has a partial pressure p_{partial}, $\Delta\omega_j$ is scaled using the following equation:

$$\Delta\omega_j(p,T) = \left(\frac{T_{\text{ref}}}{T}\right)^{n_{\text{air}}} (\Delta\omega_{j,\text{air}}(p_{\text{ref}}, T_{\text{ref}})(p - p_{\text{i,partial}}) + \Delta\omega_j(p_{\text{ref}}, T_{\text{ref}})p_{\text{i,partial}}). \tag{13}$$

In addition, the air-broadened half-intensity width $\Delta\omega_{j,\text{air}}$ is required, which takes into account the influence of air molecules on the width of the spectral line. The temperature dependence of this half-width is described by the coefficient n_{air}.

To understand how temperature affects the refraction of gas, the air components nitrogen and oxygen from Section II-A were selected. The temperature was first increased to 50 °C and then to 100 °C. As shown in (11) and (13), the intensity and half-width of the spectral resonance lines change with temperature. In addition, the ideal gas law, which describes the behavior of ideal gases under varying conditions, must be considered

$$p \cdot V = \rho \cdot R \cdot T \tag{14}$$

where V represents the volume, ρ is the number of particles, and R corresponds to the universal gas constant. Applying this to our case, the heat from the exothermic reaction causes the gases to rise and expand. However, since this is not a closed system, the existing pressure remains the same. As a result, there are significantly fewer molecules in the volume under consideration, leading to a decrease in the refractivity of the gases. This can be observed for individual components such as O_2 and N_2 in Fig. 3.

In the case of humid air, with a relative humidity of 50%, there is an increase in refractivity. The ideal gas law also applies in this case, resulting in a decrease in density of the gas. However, as the temperature rises, the proportion of humidity increases. This phenomenon can be attributed to the rising concentration of water in the air mixture. As the temperature rises, the water vapor saturation pressure increases, thereby enhancing the capacity of the air to absorb water vapor. At a temperature of 20 °C, the ambient air can absorb a maximum of 2.31% water at 101 325 Pa. However, as the temperature rises to 50 °C, the maximum amount of water vapor in the air increases to 12%. As the proportion of water vapor increases, the reduction in refractivity caused by the gas becoming less dense is reversed. As water vapor is the primary contributor to the refractive index, the refractive index of humid air increases considerably, as can be seen in Fig. 4. The studies conducted by [27] validate the model by measuring the air for various humidity and temperature values in the W-band and comparing the results. As previously discussed, a portion of the product of exothermic reactions is water, which can be absorbed significantly more readily when the environment is heated, thereby increasing the refractivity in the event of a fire.

III. Setup

A. Radar-Sensor

We are using a noncommercial monostatic radar sensor from the Ruhr University Bochum. It operates in the frequency range from 70 to 90 GHz [28], [29] and it achieves a ranges resolution of 7.5 mm. It has an integrated high-frequency voltage-controlled oscillator (VCO), stabilized by a high-precision external crystal reference source with a high-precision phase locked loop. In the used monolithic microwave integrated circuit (MMIC), the signal is fed to a microstrip line via bonding wires, and then a coupling through the substrate passes the signal into a rectangular waveguide. After passing the waveguide, the signal was coupled into a dielectric lens antenna made from polytetrafluoroethylene (PTFE), shown in Fig. 5. The antenna excites plane wave fronts and possesses an 3-dB opening angle of 5.5°–6° in the e-plane and the h-plane, respectively, and has a gain of 31 dBi [30]. In our monostatic setup, it is used as transmitting and receiving antenna. All the properties are listed in Table III.

The evaluation of the radar signals can be done in two ways. The intermediate frequency signal of the received downmixed signal at the output of the sensor can be determined either via

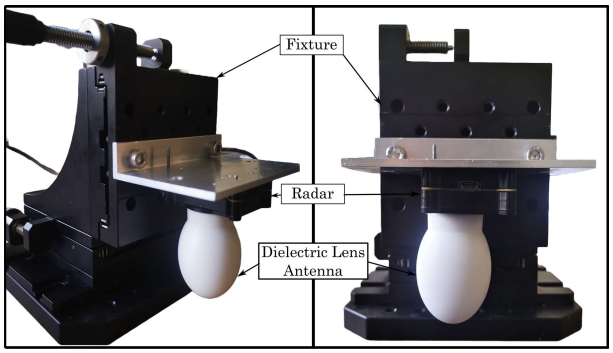

Fig. 5. Side and front views of the radar sensor with fixture and dielectric lens antenna.

TABLE III
CHARACTERISTICS OF RADAR SENSOR AND ANTENNA

W-Band Radar	
Start frequency	70 GHz
Stop frequency	90 GHz
Operation mode	monostatic
T_{ramp}	4.1 ms
Measurement frequency	100 Hz
Range resolution	7.5 mm
Doppler resolution	0.0374 Hz
Number of samples	4096
Antenna	
Material	PTFE
Opening angle azimuth	5.5°
Opening angle elevation	6°

the intermediate frequency f_{IF} or via the resulting phase ϕ_{IF}.

$$f_{\text{IF}}(\tau) = \frac{B}{T_{\text{ramp}}}\tau \tag{15}$$

$$\phi_{\text{IF}}(\tau) = 2\pi f_{\text{min}}\tau. \tag{16}$$

Here, f_{min} is the start frequency of the emitted frequency ramp, B is the bandwidth of the system, and T_{ramp} is the ramp duration and the time of flight (TOF), also known as the round-trip time of the emitted signal, $\tau = 2R_{\text{target}}/c_{\text{m}}$, with c_{m} the speed of light in a specific medium and R_{target} the distance of an object that can be determined. The reason for higher accuracy of the phase evaluation is illustrated by the Cramer–Rao lower bound (CRLB). The CRLB represents the lower limit of the variance of a mean-free estimator. The mean value becomes smaller the closer the estimator comes to the CRLB. A In short, however, the accuracy of phase-based signal processing depends on the starting frequency and not the bandwidth of the system. In absolute values, a high start frequency is much easier to achieve in terms of hardware than a high bandwidth. As a result, the phase-based approach allows a significantly more sensitive measurement approach, which can measure the smallest dielectric changes on the measurement path. A purely phase-based signal processing results in a very small unambiguity range at a high start frequency. Therefore, a combined signal processing consisting of frequency-based and phase-based signal processing is used. The frequency-based part limits the unambiguity range and also allows measuring at a large distance. In the second step, this unambiguity range is used to apply the phase-based algorithm to measure the small changes in the measurement

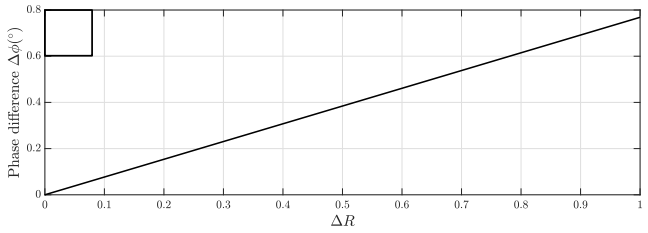

Fig. 6. Change in phase in degrees as a function of the change in refractivity over a measuring distance of 0.4 m.

path. An exact description of the derivation and implementation of the signal processing can be found in [32] and [33]. According to the measurement concept, a measurement is first carried out against a fixed target, without smoke on the measuring path. In signal processing, the phase ϕ_{air} of the fixed target is evaluated as reference. In the second step, smoke occurs in the measurement path. The relative permittivity is the refractive index of the air on the measuring section changes and thus also the evaluated phase of the solid target ϕ_{smoke}. By comparing the two measurements and calculating the difference between the two measurement scenarios, it is possible to calculate how much the dielectric properties of the measurement section changed. With the phase difference $\Delta\phi$ and the known measurement path R_{fire}, it can be calculated as

$$\Delta\phi = 360° \frac{f_{\text{min}}}{c_0} \cdot (n_{\text{air}} - n_{\text{smoke}}) \cdot 2R_{\text{fire}}. \tag{17}$$

If the difference between the two refractive indices is now combined to Δn, the change in the refractive index can now be determined via the phase difference

$$\Delta n = \frac{\Delta\phi \cdot c_0}{360° \cdot f_{\text{min}} \cdot 2R_{\text{fire}}}. \tag{18}$$

In Fig. 6, the difference in the refractive index Δn was changed from 0.0000001 to 0.000001 or in terms of the refractivity $\Delta R = 1$. This corresponds to a change in a pretty early stage of the room in [20]. This means that a change in the refractivity with $\Delta R = 1$ would result in a phase difference of 0.78°. A change of 0.5° in the measured phase corresponds to a change in the refractive index of 0.0000065 over a measurement distance of 1 m. Investigations in [12] show that the standard deviation (STD) of the radar used here is significantly lower, thus enabling measurements within the range of 0.5°. This allows for the detection of smoke development at its earliest stages and provides insights into the nature of the fire based on how the phase changes over time.

B. Fire Detection Laboratory

1) Laminar Flow Measurements in a Smoke Duct: In this scenario, well-defined laminar smoke is generated in a controlled smoke duct environment. This setup allows for precise measurement of the dielectric properties of smoke using FMCW radar sensors. The controlled nature of the laminar flow ensures consistent and repeatable conditions, providing reliable data on how smoke affects radar signal propagation. “EN 54 Fire detection and fire alarm systems” is a series of European standards covering product standards and application guidelines for fire detection, fire alarm, and voice alarm systems. Standard EN54-7 specifies the properties for a

smoke duct and different kinds of test fire to ensure repeatable and reproducible measurements for testing point-type smoke detectors. For the purpose of this work, we used the smoke duct of the Heinz–Luck fire detection laboratory at the University of Duisburg-Essen, Germany. The smoke duct must contain a working space in which the air temperature and air flow correspond to the required test conditions. Essentially, a laminar air flow with the required velocities of 0.2 or 1 m/s must be achieved. The turbulent air flow of the fan is guided through an air rectifier to approximate a laminar flow. To ensure an increasing aerosol density, a closed-circuit setup was constructed. The flow area of the duct measures 0.4 × 0.4 m. To determine the increasing aerosol density, an extinction measuring device MIREX, according to EN5-7, is used in the working chamber [34]. The system operates by emitting infrared light, which is then directed across a distance of 2 m and reflected by a mirror. Subsequently, the system receives and measures the light extinction at a localized position, covering a width of 1 m. The MIREX system has been developed for the purpose of evaluating the efficacy of smoke detectors under a variety of controlled circumstances. As a consequence, it represents an exacting standard against which the performance of new sensors for smoke detection technologies can be assessed. At the same time, a PT100 resistor is used to determine the working operating temperature in the working chamber. An illustration of the entire smoke duct and the inlet for the aerosol generator can be found in Fig. 7. A paraffin oil aerosol generator from Lorenz (AGW-R/BM VI) is used for aerosol production. This generator can adjust the concentration, the output volume flow, and the particle size distribution. The radar sensor was placed at the lower part of the duct. The measuring path passes through a hole in the metal wall. This hole was covered with a Styrofoam plate to protect the antenna from the smoke. The total length of the measuring path is 45 cm. The opposite metal wall serves as a fixed target. When aligning the radar sensor, it was ensured that the maximum reflection strength was measured at the wall.

2) Smoke Generator in an Open Room for Turbulent Flow Measurements: This setup involves using a smoke generator in an open room to create turbulent smoke flow. The turbulent flow profile better simulates real-life scenarios where smoke behaves unpredictably. Phase-based radar measurements are used to observe the behavior of the ascending smoke over time, offering insights into the complex interactions between turbulent smoke and electromagnetic waves.

3) TFs in a Fire Detection Laboratory for Smoke Measurements as a Realistic Scenario: Two TFs are ignited in a fire detection laboratory to study smoke in conditions that closely mimic actual fire events. The radar sensor measures the rising smoke above the fire, and the phase pattern over time is analyzed to draw conclusions about the combustion behavior of the fire. The TFs for turbulent flow measurements were performed in a fire test room with a floor area of 10.5 × 9.0 m and two adjacent observation rooms in which the radar sensor was positioned in front of a dielectric window. The ceiling of the fire test room is height-adjustable via a spindle lifting gear and allows the room height to be set from 2.90 to 6.60 m. For this test, the ceiling was moved to a height of 5.65 m. The fire was lit in the middle of the room. Two TFs were ignited: TF4, in which plyurethane foam was burned,

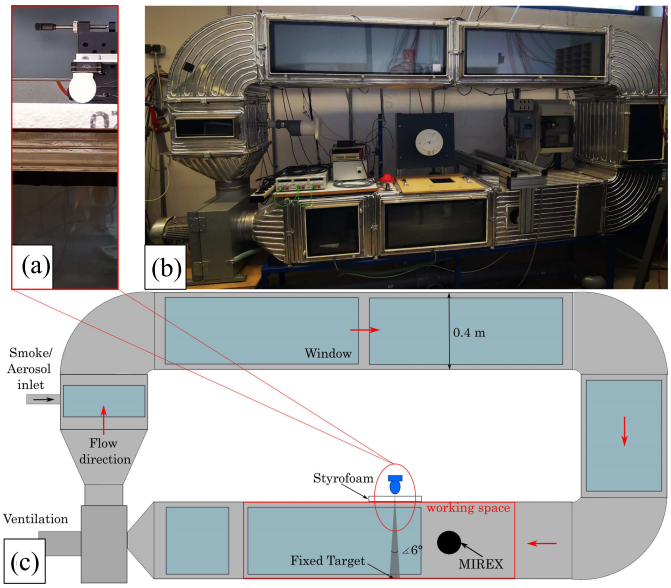

Fig. 7. (a) Frontal view of the smoke duct. (b) Top view of the positioning unit of the aerosol generator. (c) Feed-through of the positioning unit of the generator.

and TF5, in which liquid n-heptane was ignited. A detailed overview of the fire tests can be found in [12] and [13]. The TF4 and TF5 were chosen because they were open fires with strong flame development. At the same time, both fires produce smoke, although to different degrees. The large flame development guarantees a turbulent thermal behavior of the air, and at the same time it can be investigated how different strong smoke development behaves on the measurements. The current European standard EN54 (Part 7) provides all information for TF4 and TF5. In all test scenarios, the fire material was positioned centrally, approximately 45 cm above the ground. When necessary, it was contained within designated containers. To collect comprehensive data as a well-known reference for these tests, we used a well-established MIREX measurement system [34]. As a further reference parameter, we have determined the temperature via a PT1000 measuring resistor. The MIREX system and the PT1000 resistor are positioned at a radius of 3 m around the fire. They are located directly below the ceiling; more precisely, the MIREX system is located 10 cm below the ceiling and the PT1000 resistor is located just under 2 cm below the ceiling. From the radar sensor's point of view, the fire is directly in front of the radar. The other two sensors are located approximately 1.9 m to the left of the radar.

C. MIREX

The well-established MIREX measurement system operates by emitting infrared light, which is then directed across a distance of 2 m in the test fire laboratory and over 0.4 m in the smoke duct, and then reflected by a mirror. Subsequently, the system receives and measures the light extinction coefficient m_{ext}

$$m_{\text{ext}} = \frac{10}{l} \cdot \log_{10}\left(\frac{I_0}{I_{\text{e}}}\right) \tag{19}$$

where m_{ext} is a function of the measurement length l, I_0 is the incident laser intensity measured prior to the introduction

of the smoke flow into the duct, and I_r is the transmitted laser intensity

$$I_r = I_0 \cdot e^{-\sigma_{ext} l}. \tag{20}$$

The laser intensity I_r during the smoke measurements depends on the number of particles ρ and the extinction coefficient σ_{ext}

$$\sigma_{ext} = \rho \cdot c_{ext}. \tag{21}$$

Here, c_{ext} is the cross section of the particles. Since the diameter of the particles is in the same order of magnitude as the wavelength of the laser, c_{ext} can be calculated using the Mie solution [35]. Now (19) and (20) can be used to determine the number of particles ρ in the smoke

$$\rho = \frac{\ln(10)}{10} \cdot \frac{m_{ext}}{c_{ext}}. \tag{22}$$

Assuming spherical particles and knowing that the particle size can be set using an adjustable aerosol generator, the Mie scattering of the particles for the wavelength of 900 nm can be determined using a custom-written simulation program [36]. For instance, if the measured value m_{ext} increases to 1dB/m, it results in a number of 273046710 319 /m^3 particles with a particle diameter of 0.70295 μm, which corresponds to a volume fraction of 0.04966 ppm.

IV. Results

A. Laminar Flow Measurements

This section provides an explanation of the measurement results obtained during the smoke duct experiment. For this purpose, the fan was set to a speed of 0.2 m/s and the standard particle size distribution was set. The smoke density was increased linearly over 550 s, reaching a maximum particle volume fraction of 0.46512 ppm. The particle density value was measured with the MIREX at a measurement frequency of 48 Hz. The particle density can be deduced from the absorbed strength of the signal. Fig. 8 shows the absorption strength in dB/m. Over the same period, 40 000 measurement ramps of the radar sensor were emitted and received at a measurement frequency of 100 Hz. In each measurement, the distance to the fixed target was determined and the corresponding phase was calculated.

Fig. 8 shows the determined phase values over time. The diagram is divided into two scenarios: the first 5000 measurements were taken before the generator was switched on, where the phase values were stable at 162.25°, with an STD of 0.0585°. The next 40 000 measurements were taken while the generator was on, showing that the phase increased with the density, but the phase fluctuations did not increase. This indicates that the laminar gas flow in the smoke duct showed no significant fluctuations in density, maintaining a consistent phase measurement from the radar over time.

A laser-based system, the MIREX, was used to determine the smoke density, and it showed a similar response to the increasing smoke concentration. Both the sensors exhibited analogous trends as the smoke density increased linearly. The slopes of the measurements from both the sensors were comparable, highlighting the consistency between the radar- and laser-based systems.

Table IV summarizes the calculated changes for different time frames, focusing on the changes in the measured phase

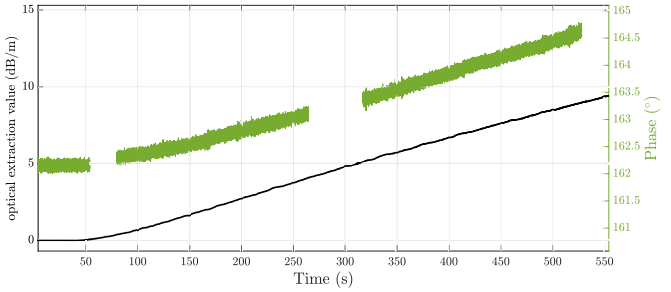

Fig. 8. Measurement of the increasing smoke density in the smoke channel, with the phase values of the radar sensor in green and the extraction values of the MIREX in black.

TABLE IV
Calculated Changes for Different Time Frames for the Measured Phase, Extraction Value m_{EXT}, Volume Fraction ζ, and Refractivity R

Time-Frame	$\Delta\phi$ in °	Δm_{ext} dB/m	$\Delta\ \zeta$ ppm	ΔR via Radar
80-180	0.40	1.938	0.09624	4.9
180-280	0.42	2.066	0.10260	4.9
317-417	0.41	1.935	0.096092	4.9
417-517	0.35	1.821	0.090431	3.7

of the radar, the MIREX extraction value, the calculated volume fraction, and the calculated refractivity. The refractivity was determined through the measured phase of the radar sensor. For example, during the time frame of 80–180 s, the phase change was 0.4°, the extraction value change was 1.938 dB/m, the volume fraction change was 0.09624 ppm, and the refractivity change was 4.9. These values indicate that as the particle volume fraction increases, the refractivity changes correspondingly.

B. Turbulent Flow Measurements

In this section, we focus on analyzing the phase patterns measured over time and their application in characterizing combustion behavior. The phase pattern of a signal can provide insights into the presence of a flame, hot air, or rising gases. As discussed in Section II, smoke can be described as a changing dielectric material. Consequently, it affects the speed of propagation and the TOF of the signal. We start with the second measurement scenario, where an aerosol mixture similar to that used in the smoke duct for laminar flow measurements is used to ensure comparability. In this case, the smoke produced by an aerosol generator is allowed to rise naturally. Measurement series of 100 s were conducted, with no aerosol generated for the first 12 s. After that, smoke was released for about 3 s and then spread throughout the room. After 100 s, the room was ventilated again. This pattern can also be seen in the measured radar data. During the first 12 s, the measured phase is very stable, with an STD of 0.05° over 2000 measurement ramps. When the aerosol generator is turned on for 3 s, the phase increases abruptly due to dense smoke ejection, as seen in Fig. 9. Afterward, the measured phase decreases quickly but not linearly; slight fluctuations can be observed from 20 to 50 s. Here, the smoke expands in the room nonlinearly and nonhomogeneously, resulting in dense fluctuations. After 50 s, the fluctuations become smaller, and

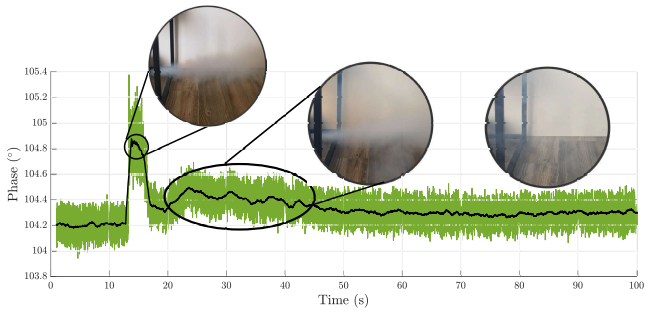

Fig. 9. Measured phase values of the radar sensor over a period of 100 s, as well as three images of the smoke produced at different stages.

the phase approaches its original value as the smoke becomes more homogeneous and loses density.

We will now take a closer look at the last measurement scenario. As mentioned above, two TFs are ignited and the rising smoke plumes are measured with the radar sensor. We can now measure not only the unpredictable expansion of the smoke as in measurement scenario two but also the thermal effects that intensify the turbulent flows of the rising smoke. To ensure comparability with smoke detectors, the radar sensor is positioned just below the ceiling. A detailed description of the measurement scenario can be found in [13]. The entire measurement sequence lasted 900 s. A pilot flame started the fire. The TF5 fire had a combustion time of 264 s, while the TF4 fire had a combustion time of 283 s. The room was ventilated approximately 80 s after the fire when the fuels were consumed. The measurement procedure was as follows: 5000 ramps were transmitted and received at a frequency of 100 Hz. This data package was then stored, and a new series of measurements was started with another 5000 ramps. Consequently, 50-s segments were continuously recorded at different time intervals. As smoke rises, the phase pattern displays significant noise and variations. The mean value of the measured phase sometimes increases or decreases due to dense fluctuations and irregular smoke expansion. Over time, as the smoke dissipates, the phase returns to its original value.

The measurement results for the TF5 fire are shown in Fig. 10, with three photographs taken at different times (90, 280, and 310 s). Fig. 10(a) shows the MIREX extraction values in dB/m, representing the particle density in the room (red) and the combustible weight (black) over time. The temperature (red) and the measured phase (multicolored) are shown in Fig. 10(b). To emphasize measurement trends, a moving average over 100 values is shown in black. Table V provides an overview of time slots (TF5-1 to TF5-4), including the time range, smallest and largest measured phase values, mean value over 5000 measurements, and STD for the specified time range. The measurement results for the TF4 fire are presented and discussed in Fig. 11 and Table VI, following the same structure as the TF5 measurements. Fig. 11 features photographs of the flame at different times (100, 180, 220, and 280 s). These photographs suggest a different combustion process for TF4 compared with TF5. Initially, the pilot flame in the right front corner of the container ignites the PU foam. Over time, the flame spreads until the entire foam is on fire. After the peak, the flame gradually moves to the right side of the mat, eventually extinguishing in the rear right-hand corner. Considering the individual time slots, it is easy to

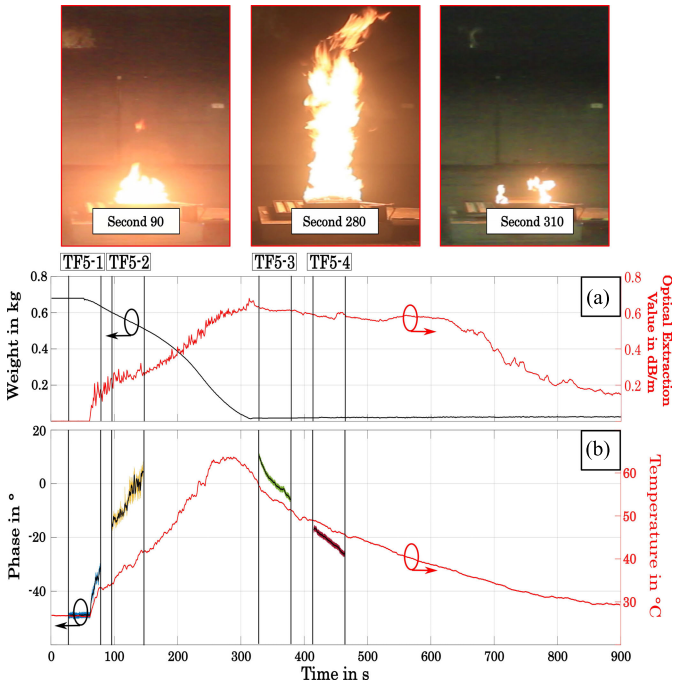

Fig. 10. TF5—Fire. (a) Comparison of the fuel weight (black) and the MIREX optical absorption measurements (red). (b) Comparison of the radar measurements (black) and the PT1000 temperature measurements (red).

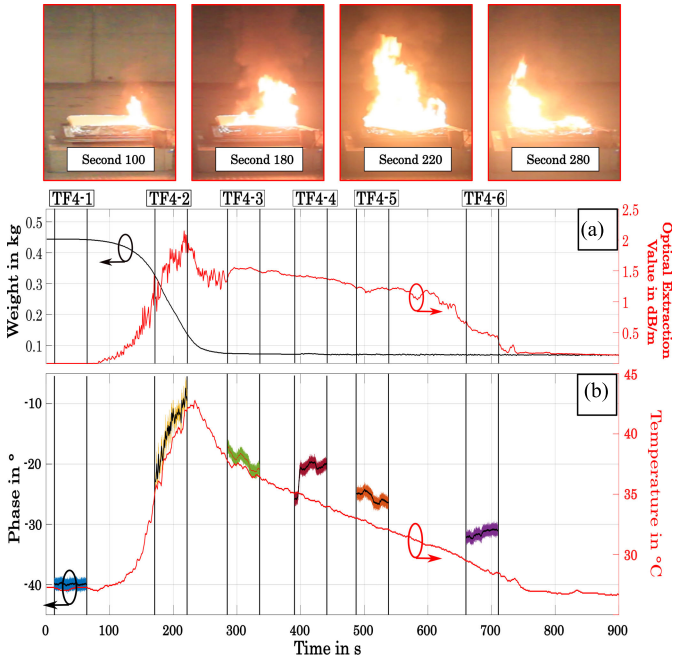

Fig. 11. TF4—Fire. (a) Comparison of the fuel weight (black) and the MIREX optical absorption measurements (red). (b) Comparison of the radar measurements (black) and the PT1000 temperature measurements (red).

observe in TF5-1 how the smoke detection starts, with the phase increasing significantly after 61 s. In TF5-2 and TF4-2, it is evident that the underlying fire exhibits very fluctuating behavior, leading to increased phase fluctuation. This not only indicates the presence of smoke but also provides valuable information on the dynamics of the fire. Even though the flames or fire are not directly within the radar sensor's field of view, the radar can detect changes in the smoke patterns. A comparison of the measured values shows that the phase of

TABLE V
MEASURED VALUES OF THE RADAR SENSOR FOR THE TF5

Time-Frame	Time in s	Phase-Max	Phase-Min in	Phase Avr.	Phase STD
TF5-1	21 - 71	-29.67°	-50.43°	-45.51°	5.65°
TF5-2	95 - 145	8.21°	-18.45°	-6.38°	6.23°
TF5-3	328 - 378	11.57°	-6.7°	0.88°	4.19°
TF5-4	415 - 465	-15.43°	-27.32°	-21.35°	2.85°

TABLE VI
MEASURED VALUES OF THE RADAR SENSOR FOR THE TF4

Time-Frame	Time in s	Phase-Max	Phase-Min in	Phase Avr.	Phase STD
TF4-1	12 - 62	-51.97°	-58.92°	-55.50°	1.02°
TF4-2	171 - 221	-44.61°	-60.65°	-53.59°	2.21°
TF4-3	285 - 335	-13.37°	-58.33°	-41.35°	6.40°
TF4-4	380 - 440	-25.34°	-59.62°	-45.94°	4.42°
TF4-5	488 - 538	-47.44°	-56.73°	-52.52°	1.14°
TF4-6	660 - 710	-46.32°	-56.48°	-51.73°	1.79°

the TF5 fire increases from a minimum value of $-50.43°$ to a maximum of 11.57°, resulting in a phase difference of 62°. The TF4 fire reaches a difference of 45.55°, which is significantly smaller compared with TF5. Comparing this with the values of the other sensors, this behavior correlates strongly with the heat output of the combustion [37]. The phase patterns measured during these tests were analyzed to characterize the smoke behavior. Variations in the phase patterns correspond to different stages of smoke emission and the associated combustion process, such as the presence of a flame or the emission of hot gases. By comparing the phase patterns over time, it is possible to distinguish between different behaviors of the smoke and assess the stability and intensity of the fire. This article [38] shows similar measurements on a smaller scale by performing fixed target measurements using FMCW radar sensors through an ethanol fire. A series of measurement runs were conducted with the flame being repeatedly relit. The FMCW radar sensors demonstrated consistent and reliable performance. The results indicate that phase pattern analysis can be a valuable tool in smoke detection, providing insights into the presence and nature of smoke, hot air, and rising gases. Unlike traditional smoke detectors that simply signal the presence of smoke, phase pattern analysis can offer detailed information about the fire scenario. This includes whether the fire is spreading or diminishing, which can significantly improve the accuracy of fire alarms and reduce false alarm rates. In time slot TF4-4, a sudden change in the measured phase is observed, which is caused by the activation of the ventilation system. The ventilation process plays a critical role in influencing smoke distribution and the particle mixture in the air. When the ventilation system is activated, it circulates the air, leading to a new mixture of particles, which is reflected in the phase pattern. Similarly, in time slot TF4-6, a rising phase change is observed. This change is attributable to the changes in the ventilation properties, which, at this point, caused a significant amount of material from the burning polyurethane foam to be introduced into the air. The increase in airborne combustion products altered the refractive index of the air, resulting in the observed phase shift. This behavior is consistent with the influence of the ventilation system observed in TF4-4, although the exact distribution and composition of particles at TF4-6 differed, leading to a phase change opposite to that seen in TF4-3 and TF4-5.

C. Sensor Position

The methodology for measuring and the insights gained from the measurement data demonstrate that the measurement principle used is an integral method. As the dimensions of the smoke increase, the variation in the measured phase also increases. This indicates that the positioning of the radar is of considerable consequence and necessitates further investigation. First, the height of the sensor should be addressed. For further context, see [3], in which TF4 and TF5 were ignited under identical conditions. The sensor was now situated at the same height as the flame and thus almost 2.5 m lower than in this work. A comparison of the measurement data from the two studies reveals a notable discrepancy in the observed phase patterns over time. The data indicate that the measurement path may traverse either a region of smoke situated just below the ceiling or the direct path through the flame. In this scenario, these represent the two potential extremes, yet the optimal height is dependent on the intended application. In the context of smoke detection, it is reasonable to conduct measurements at a height just below ceiling level, as this is where the majority of smoke accumulates and strong phase differences can be anticipated. Similarly, the measuring position must be adjusted depending on the specific area of application. Finally, we will address the issue of the measuring angle. Given that the measurement principle is dependent on a fixed target, the objective of the alignment process should be to achieve maximum reflection, which is accomplished when the measured reflection peak is at its maximum intensity. In the event of a slight tilt angle resulting from inaccuracy, a defined spot size of the measuring beam guarantees that the beam passes through the observed smoke. Concurrently, there is a minimal extension of the measuring distance, which nevertheless exerts only a minimal influence on the phase difference and is lost in the phase fluctuation.

V. CONCLUSION

In this study, we explored the use of FMCW radar sensors operating in the 70–90-GHz range for smoke detection and fire characterization. Our research demonstrated that radar-based systems could effectively operate in smoke-filled environments where traditional optical methods often fail. By conducting controlled experiments in a smoke duct compliant with the EN54-7 standard, we precisely measured the dielectric properties of smoke and analyzed its impact on radar signal performance. While commercial smoke detectors on the market will always be more effective for the primary detection of smoke, radar-based systems offer significant advantages beyond detection. Specifically, radar can continue to provide valuable information in environments where smoke density reaches levels that would limit the effectiveness of optical sensors. The key findings from our experiments with laminar flow in a smoke duct, turbulent flow from a smoke generator, and real TFs demonstrated the versatility and effectiveness of radar sensors. Unlike conventional smoke detectors, radar-based measurements can go beyond simple detection by

providing real-time insights into the fire's dynamics, such as whether it is spreading or diminishing. Furthermore, the phase pattern analysis can significantly improve the accuracy of fire alarms and reduce false alarm rates, leading to more informed and timely decision-making in emergency situations. The activation of ventilation systems and their impact on smoke dispersion were also examined, revealing how changes in the particle mixture could be monitored through phase pattern shifts. By combining radar technology with traditional smoke detectors, emergency response teams could receive not only an initial fire alarm but also continuous, detailed information about the fire's progression. Overall, our findings suggest that millimeter-wave radar technology holds great potential for enhancing smoke detection and fire characterization. Future work should focus on integrating radar-based systems with other sensory technologies to develop comprehensive solutions for real-time smoke detection and monitoring. In addition, further research is needed to refine these technologies for broader application in various fire scenarios, ultimately improving safety and effectiveness in emergency management. In conclusion, while radar technology is not intended to replace existing smoke detectors, it provides an invaluable tool for collecting additional information in situations where smoke density inhibits optical sensors. This makes radar an ideal complement to traditional systems, offering a diverse and redundant solution for improved fire detection and characterization.

ACKNOWLEDGMENT

The authors would like to express their gratitude to Prof. Nils Pohl and his team for providing the high-performance radar system.

REFERENCES

[1] S. Festag, *False Alarm Study: False Alarm Data Collection and Analysis from Fire Detection and Fire Alarm Systems in Selected European Countries*. Berlin, Germany: Erich Schmidt Verlag, 2018.

[2] T. Schultze, T. Kempka, and I. Willms, "Audio-video fire-detection of open fires," *Fire Saf. J.*, vol. 41, no. 4, pp. 311–314, Jun. 2006, doi: 10.1016/j.firesaf.2006.01.002.

[3] V. Bianco, M. Paturzo, A. Finizio, K. A. Stetson, and P. Ferraro, "Portable IR laser system for real-time display of alive people in fire scenes," *J. Display Technol.*, vol. 11, no. 10, pp. 834–838, Oct. 2015.

[4] P. Fritsche, B. Zeise, P. Hemme, and B. Wagner, "Fusion of radar, LiDAR and thermal information for hazard detection in low visibility environments," in *Proc. IEEE Int. Symp. Saf., Secur. Rescue Robot. (SSRR)*, Shanghai, China, Oct. 2017, pp. 96–101.

[5] A. Bystrov, L. Daniel, E. Hoare, F. Norouzian, M. Cherniakov, and M. Gashinova, "Comparative analysis of 300 GHz and 79 GHz radar performance in fire environments," in *Proc. IEEE Radar Conf. (RadarConf)*, Sep. 2020, pp. 1–4.

[6] A. Bystrov, L. Daniel, E. Hoare, F. Norouzian, M. Cherniakov, and M. Gashinova, "Experimental evaluation of 79 GHz radar performance in fire environments," in *Proc. 21st Int. Radar Symp. (IRS)*, Oct. 2020, pp. 202–204.

[7] A. Batra et al., "Millimeter wave indoor SAR sensing assisted with chipless tags-based self-localization system: Experimental evaluation," *IEEE Sensors J.*, vol. 24, no. 1, pp. 844–857, Jan. 2024.

[8] T. Kubiczek and J. C. Balzer, "Material classification for terahertz images based on neural networks," *IEEE Access*, vol. 10, pp. 88667–88677, 2022.

[9] S. Abouzaid, T. Jaeschke, S. Kueppers, J. Barowski, and N. Pohl, "Deep learning-based material characterization using FMCW radar with open-set recognition technique," *IEEE Trans. Microw. Theory Techn.*, vol. 71, no. 11, pp. 1–11, Nov. 2023.

[10] J. Barowski, M. Zimmermanns, and I. Rolfes, "Millimeter-wave characterization of dielectric materials using calibrated FMCW transceivers," *IEEE Trans. Microw. Theory Techn.*, vol. 66, no. 8, pp. 3683–3689, Aug. 2018.

[11] A. A. Pramudita et al., "Radar system for detecting respiration vital sign of live victim behind the wall," *IEEE Sensors J.*, vol. 22, no. 15, pp. 14670–14685, Aug. 2022.

[12] F. Schenkel, T. Schultze, C. Baer, I. Rolfes, and C. Schulz, "Radar-enabled millimeter-wave sensing of fire interactions," *IEEE Trans. Instrum. Meas.*, vol. 73, pp. 1–10, 2024.

[13] F. Schenkel, T. Schultze, C. Baer, I. Rolfes, and C. Schulz, "Radar-based smoke detection at millimeter wave frequencies: An experimental study," in *IEEE MTT-S Int. Microw. Symp. Dig.*, Jun. 2024, pp. 887–890.

[14] G. E. Gorbett and S. P. Kozhumal, *Fire Fundamentals*. Cham, Switzerland: Springer, 2023, pp. 55–100, doi: 10.1007/978-3-030-94356-1_3.

[15] A. R. Von Hippel, *Dielectric Materials and Applications*. Norwood, MA, USA: Artech House, 1995.

[16] P. Debye, *Polare Molekeln*. Stuttgart, Germany: Verlag von S. Hirzel, 1929. [Online]. Available: https://books.google.de/books?id=tB06AQAAIAAJ

[17] L. S. Rothman et al., "The Hitran 2004 molecular spectroscopic database," *J. Quant. Spectrosc. Radiat. Transf.*, vol. 96, no. 2, pp. 139–204, 2005. [Online]. Available: https://www.sciencedirect.com/science/article/pii/S0022407305001081

[18] D. Grischkowsky, Y. Yang, and M. Mandehgar, "Zero-frequency refractivity of water vapor, comparison of Debye and van-vleck weisskopf theory," *Opt. Exp.*, vol. 21, no. 16, p. 18899, Aug. 2013. [Online]. Available: https://opg.optica.org/oe/abstract.cfm?URI=oe-21-16-18899

[19] B. Hattenhorst, L. Piotrowsky, N. Pohl, and T. Musch, "An mmWave sensor for real-time monitoring of gases based on real refractive index," *IEEE Trans. Microw. Theory Techn.*, vol. 69, no. 11, pp. 5033–5044, Nov. 2021.

[20] P. Basmer and Z. Gerhard, "Einsatzmöglichkeiten eines mobilen Ft-IR-gasanalysators," Forschungsstelle für Brandschutztechnik, Universität Karlsruhe und Ansyco Karlsruhe, Karlsruhe, Deutschland, Tech. Rep. Forschungsbericht 137, Sep. 2024.

[21] F. W. Heineken and F. Bruin, "Some measurements on refractive indices of gases in the microwave region," *Physica*, vol. 20, nos. 1–6, pp. 350–360, 1954. [Online]. Available: https://www.sciencedirect.com/science/article/pii/S0031891454800498

[22] C. Baer, T. Jaeschke, N. Pohl, and T. Musch, "Contactless detection of state parameter fluctuations of gaseous media based on an mm-wave FMCW radar," *IEEE Trans. Instrum. Meas.*, vol. 64, no. 4, pp. 865–872, Apr. 2015.

[23] C. Baer, T. Jaeschke, P. Mertmann, N. Pohl, and T. Musch, "A mmWave measuring procedure for mass flow monitoring of pneumatic conveyed bulk materials," *IEEE Sensors J.*, vol. 14, no. 9, pp. 3201–3209, Sep. 2014.

[24] T. Baum, L. Thompson, and K. Ghorbani, "A complex dielectric mixing law model for forest fire ash particulates," *IEEE Geosci. Remote Sens. Lett.*, vol. 9, no. 5, pp. 832–835, Sep. 2012.

[25] A. Sihvola, *Electromagnetic Mixing Formulas and Applications* (IEE Electromagnetic Waves Series). New York, NY, USA: Institution of Electrical Engineers, 1999. [Online]. Available: https://books.google.de/books?id=uIHSNwxBxjgC

[26] L. S. Rothman et al., "HITEMP, the high-temperature molecular spectroscopic database," *J. Quant. Spectrosc. Radiat. Transf.*, vol. 111, no. 15, pp. 2139–2150, Oct. 2010. [Online]. Available: https://www.sciencedirect.com/science/article/pii/S002240731000169X

[27] J. Mahendran, F. Schenkel, I. Rolfes, and C. Schulz, "Radar-based investigation of electromagnetic waves under different temperature and humidity conditions," in *Proc. Int. Conf. Electromagn. Adv. Appl. (ICEAA)*, Sep. 2024, pp. 603–607.

[28] N. Pohl, T. Jaeschke, and K. Aufinger, "An ultra-wideband 80 GHz FMCW radar system using a SiGe bipolar transceiver chip stabilized by a fractional-N PLL synthesizer," *IEEE Trans. Microw. Theory Techn.*, vol. 60, no. 3, pp. 757–765, Jan. 2012.

[29] N. Pohl, T. Jaeschke, S. Küppers, C. Bredendiek, and D. Nüßler, "A compact ultra-wideband mmWave radar sensor at 80 GHz based on a SiGe transceiver chip (focused session on highly-integrated millimeter-wave radar sensors in SiGe BiCMOS technologies)," in *Proc. 22nd Int. Microw. Radar Conf. (MIKON)*, May 2018, pp. 345–347.

[30] N. Pohl and M. Gerding, "A dielectric lens-based antenna concept for high-precision industrial radar measurements at 24 GHz," in *Proc. 9th Eur. Radar Conf.*, Oct. 2012, pp. 405–408.

[31] S. Scherr, S. Ayhan, M. Pauli, and T. Zwick, "Accuracy limits of a K-band FMCW radar with phase evaluation," in *Proc. 9th Eur. Radar Conf.*, Oct. 2012, pp. 246–249.
[32] F. Schenkel, C. Baer, I. Rolfes, and C. Schulz, "Plasma state supervision utilizing millimeter wave radar systems," *Int. J. Microw. Wireless Technol.*, vol. 15, no. 6, pp. 1001–1011, Jul. 2023.
[33] L. Piotrowsky, T. Jaeschke, S. Kueppers, J. Siska, and N. Pohl, "Enabling high accuracy distance measurements with FMCW radar sensors," *IEEE Trans. Microw. Theory Techn.*, vol. 67, no. 12, pp. 5360–5371, Dec. 2019.
[34] *Extinction Measuring Equipment MIREX*, CERBERUS LTD, New York, NY, USA, 1991.
[35] H. Hulst and H. van de Hulst, *Light Scattering by Small Particles* (Dover Books on Physics). New York, NY, USA: Dover, 1981. [Online]. Available: https://books.google.de/books?id=6ivW_TgIdjIC
[36] T. Schultze, "Untersuchungen zur minderung von durch Störaerosole bedingten fehlalarmen bei optischen rauchmeldern," Ph.D. Dissertation, Faculty Eng., Dept. Elect. Eng. Inf. Technol., Univ. Duisburg-Essen, Duisburg/Essen, Germany, 2010. [Online]. Available: https://nbn-resolving.org/urn:nbn:de:hbz:464-20110117-144051-1
[37] W. L. Grosshandler, "Towards the development of a universal fire emulator-detector evaluator," *Fire Saf. J.*, vol. 29, nos. 2–3, pp. 113–127, Sep. 1997, doi: 10.1016/s0379-7112(96)00031-8.
[38] F. Schenkel, C. Baer, I. Rolfes, and C. Schulz, "Flame-millimeter-wave-interactions: A radar-based sensor concept," in *Proc. IEEE Sensors Appl. Symp. (SAS)*, Jul. 2023, pp. 1–5.

Francesca Schenkel (Graduate Student Member, IEEE) received the M.Sc. degree in electrical engineering from Ruhr University Bochum, Bochum, Germany, in 2020, where she is currently pursuing the Ph.D. degree in electrical engineering at the Institute of Microwave Systems.

Since 2020, she has been a Research Assistant with the Institute of Microwave Systems, Ruhr University Bochum. Her current research interests include radar systems, material characterizations, antenna design, and high-temperature measurements.

Thorsten Schultze received the Diploma and Ph.D. degrees in electrical engineering, from the University of Duisburg–Essen, Duisburg, Germany, in 2003 and 2010, respectively.

He is currently working as an Academic Senior Councillor (Akademischer Oberrat) with the Chair of Communication Systems, University of Duisburg-Essen. His main research interests include automatic fire detection technologies and broadband microwave and THz analyses for fire and security break applications.

Christoph Baer (Senior Member, IEEE) received the Dipl.-Ing. and Dr.-Ing. degrees in electrical engineering from Ruhr University Bochum, Bochum, Germany, in 2009 and 2015, respectively.

From 2006 to 2015, he was an RF Research Engineer with the Krohne Group, Duisburg, Germany. In 2016, he became an Academic Councillor and a Lecturer. Since 2022, he has been an Academic Senior Councillor with the Institute of Electronic Circuits, Ruhr University Bochum. He has authored or co-authored more than 100 scientific papers and holds several patents. His current fields of research concern radar components and systems, humanitarian technology, antenna design, and microwave material characterization and synthesis.

Dr. Baer is the Vice-Chair of IEEE Germany Section (2021–2022) and the Founder of IEEE SIGHT Germany Section.

Jan C. Balzer (Member, IEEE) received the Dipl.-Ing. (FH) degree in telecommunications from Dortmund University of Applied Sciences, Dortmund, Germany, in 2008, and the Master of Science degree in electrical engineering and information technology and the Dr.-Ing. degree from Ruhr University Bochum, Bochum, Germany, in 2010 and 2014, respectively.

In 2015, he has joined the Research Group of Prof. Martin Koch, Philipp University of Marburg, Marburg, Germany, as a Post-Doctoral Fellow. Since 2017, he has been an Assistant Professor of terahertz systems with the Faculty of Engineering, University of Duisburg-Essen, Duisburg, Germany. His scientific research focuses on ultrafast semiconductor lasers. From here, he moved to the field of terahertz radiation generation and applications. He made contributions in the field of compact laser diode-driven THz systems, 3-D-printed THz devices, high-resolution THz imaging, and THz material characterization.

Ilona Rolfes (Senior Member, IEEE) received the Dipl.-Ing. and Dr.-Ing. degrees in electrical engineering from Ruhr University Bochum, Bochum, Germany, in 1997 and 2002, respectively.

From 1997 to 2005, she was with the High Frequency Measurements Research Group, Ruhr University Bochum, as a Research Assistant. From 2005 to 2009, she was a Junior Professor with the Department of Electrical Engineering, Leibniz University Hannover, Hannover, Germany, where she became the Head of the Institute of Radio frequency and Microwave Engineering in 2006. Since 2010, she has been leading the Institute of Microwave Systems, Ruhr University Bochum. Her fields of research concern high-frequency measurement methods for vector network analysis, material characterization, noise characterization of microwave devices, and sensor principles for radar systems.

Dr. Rolfes is a member of the Executive Committee of IEEE MTT-S International Microwave Workshop Series on Advanced Materials and Processes. She is also a Board Member of German IEEE MTT-AP Chapter and German Commission for Electromagnetic Metrology of International Union of Radio Science (U.R.S.I.).

Christian Schulz (Member, IEEE) received the Dipl.-Ing. and Dr.-Ing. degrees in electrical engineering from Ruhr University Bochum, Bochum, Germany, in 2009 and 2016, respectively.

From 2010 to 2016, he was a Research Assistant with the Institute of Microwave Systems, Ruhr University Bochum, where he has been a Post-Doctoral Researcher, since 2016. His current fields of research are concerned with 3-D electromagnetic field simulations, plasma diagnostics, radar systems, and antenna design.

Dr. Schulz was a recipient of IEEE Antennas and Propagation Society Doctoral Research Award in 2014 and IEEE Microwave Theory and Techniques Society (IEEE MTT-S) Graduate Fellowship Award in 2015. In 2017, he received the Gert Massenberg Award for his doctoral thesis.